



PERGAMON

Available at  
[www.ElsevierComputerScience.com](http://www.ElsevierComputerScience.com)  
POWERED BY SCIENCE @ DIRECT®

Pattern Recognition 37 (2004) 1097–1116

**PATTERN  
RECOGNITION**

THE JOURNAL OF THE PATTERN RECOGNITION SOCIETY

[www.elsevier.com/locate/patcog](http://www.elsevier.com/locate/patcog)

# A new approach to mixed pixel classification of hyperspectral imagery based on extended morphological profiles

Antonio Plaza\*, Pablo Martinez, Rosa Perez, Javier Plaza

*Neural Networks and Signal Processing Group (GRNPS), Computer Science Department, University of Extremadura, Avda. de la Universidad s/n, Caceres 10071, Spain*

Received 10 April 2003; accepted 22 January 2004

## Abstract

This paper presents a new approach to the analysis of hyperspectral images, a new class of image data that is mainly used in remote sensing applications. The method is based on the generalization of concepts from mathematical morphology to multi-channel imagery. A new vector organization scheme is described, and fundamental morphological vector operations are defined by extension. Theoretical definitions of extended morphological operations are used in the formal definition of the concept of extended morphological profile, which is used for multi-scale analysis of hyperspectral data. This approach is particularly well suited for the analysis of image scenes where most of the pixels collected by the sensor are characterized by their mixed nature, i.e. they are formed by a combination of multiple underlying responses produced by spectrally distinct materials. Experimental results demonstrate the applicability of the proposed technique in mixed pixel analysis of simulated and real hyperspectral data collected by the NASA/Jet Propulsion Laboratory Airborne Visible/Infrared Imaging Spectrometer and the DLR Digital Airborne (DAIS 7915) and Reflective Optics System Imaging Spectrometers. The proposed method works effectively in the presence of noise and low spatial resolution. A quantitative and comparative performance study with regards to other standard hyperspectral analysis methodologies reveals that the combined utilization of spatial and spectral information in the proposed technique produces classification results which are superior to those found by using the spectral information alone.

© 2004 Pattern Recognition Society. Published by Elsevier Ltd. All rights reserved.

*Keywords:* Hyperspectral imagery; Mixed pixels; Extended morphological operations; Morphological profiles; Multi-scale analysis

## 1. Introduction

Hyperspectral imaging, also known as imaging spectroscopy, is a new technique in remote sensing that generates hundreds of images, corresponding to different wavelength channels, for the same area on the surface of the earth [1]. With such spectral resolution, the ability to detect and identify individual materials or land-cover classes is greatly enhanced with regards to other techniques available, such as multispectral imaging, which typically just contains tens of images. During the past few years, a great deal of new

hyperspectral instruments have been developed for remote sensing applications. For instance, the NASA/Jet Propulsion Laboratory Airborne Visible/Infrared Imaging Spectrometer (from now abbreviated as AVIRIS) [2] covers the wavelength region from 0.4 to 2.5  $\mu\text{m}$  using 224 spectral channels at a nominal resolution of 10 nm. In the near future, the use of hyperspectral sensors on satellite platforms will produce a nearly continual stream of high-dimensional data, and this expected high data volume will require fast, unsupervised means for storage, transmission and analysis [3].

A diverse array of analysis techniques have been applied to hyperspectral imagery during the last decade [4]. They are inherently either full pixel techniques or mixed pixel techniques, where each pixel vector in a hyperspectral image records the spectral information. The underlying assumption governing full pixel techniques is that each pixel

\* Corresponding author. Tel.: +34-927-257195 (Ext. 571); fax: +34-927-257203.

E-mail address: [aplaza@unex.es](mailto:aplaza@unex.es) (A. Plaza).

vector measures the response of one predominantly underlying material at each site in a scene. In contrast, the underlying assumption governing mixed pixel techniques is that each pixel vector measures the response of multiple underlying materials at each site. Unfortunately, an image is often a combination of the two situations, where many sites in a scene are pure materials, but many others are mixtures of materials. For perspective, we briefly discuss some of the existing full pixel and mixed pixel analysis techniques, and then introduce our approach.

### 1.1. Full pixel techniques

The simplest full pixel technique for hyperspectral analysis is the method of spectral matching [5]. This approach can be effective as long as the training spectra, obtained either from a reference library or from the image itself, are properly calibrated in relation to spectra of interest and provided that the full pixel scenario is appropriate. Unfortunately, a number of the pixel vectors in the scene is likely to measure the spectral response of a mixture of materials. In addition, class label assignments provided by spectral matching algorithms are not affected by spatial neighborhoods. This may be a negative consequence for mapping applications, where consistency of class labels in localized spatial neighborhoods, a concept hereinafter termed as “spatial localization”, is important. Other full pixel methods that have been applied to hyperspectral imagery include supervised, pattern recognition-based approaches such as statistical linear discrimination [6], quadratic multivariate classifiers [7], and neural networks [8]. Unsupervised algorithms such as KMEANS and ISODATA [4,9] have also been widely used for the sake of clustering multispectral and hyperspectral imagery.

### 1.2. Mixed pixel techniques

Spectral mixture analysis (SMA) techniques have overcome some of the weaknesses of full pixel approaches by using linear statistical modeling and signal processing techniques [10–12]. They are inherently either nonlinear techniques or linear techniques. Nonlinear mixed pixel analysis involves a detailed knowledge of multiple scattering effects that may arise due to the intimate association of components residing inside each pixel [13]. Although sub-pixel nonlinear mixing can be important for some types of analysis, the effects of multiple scattering in the majority of applications are assumed to be negligible if a linear model is used [14]. The key task in linear SMA is to find an appropriate suite of pure spectral constituents—called “endmembers” in hyperspectral analysis terminology—, which are then used to estimate the fractional abundances of each mixed pixel from its spectrum and the endmember spectra by using a linear mixture model [15]. However, unless accurate ground-truth information about the materials in a scene is available, the task of identifying endmembers in a scene is not trivial. Two

main approaches have been examined in the literature for this purpose, namely interactive and automated endmember extraction techniques. The pixel purity index (PPI) method [16] is the most representative interactive approach, and consists of the following steps: First, a “noise-whitening” and dimensionality reduction step is performed by using the minimum noise fraction (MNF) transform [17]. A pixel purity score is then calculated for each point in the image cube by randomly generating  $L$  lines in the  $N$ -D space comprising the MNF transformed data. All the points in that space are projected onto the lines, and the ones falling at the extremes of each line are counted. After many repeated projections to different random lines, those pixels that count above a certain cutoff threshold  $C$  are declared “pure”. These potential endmember spectra are loaded into an interactive  $N$ -D visualization tool and rotated in real time until a desired number of endmembers,  $E$ , are visually identified as extreme pixels in the data cloud. On other hand, the N-FINDR method [18] is an automated approach that finds the set of pixels which define the simplex with the maximum volume, potentially inscribed within the dataset. First, a dimensionality reduction of the original image is accomplished by MNF. Next, randomly selected pixels qualify as endmembers, and a trial volume is calculated. In order to refine the initial volume estimate, a trial volume is calculated for every pixel in each endmember position by replacing that endmember and recalculating the volume. If the replacement results in a volume increase, the pixel replaces the endmember. This procedure, which does not require any input parameters, is repeated until there are no replacements of endmembers left. It should be noted that both PPI and N-FINDR rely on spectral properties of the data alone, neglecting the information related to the spatial arrangement of pixels in the scene.

### 1.3. Proposed approach

Our current research considers hyperspectral image analysis from a broader perspective than the individual methods listed above. Instead of focusing exclusively on the spectral information contained in the data, we focus on the analysis of spatial and spectral patterns simultaneously. The integration of spatial/spectral responses in hyperspectral analysis has been identified as a requested objective in the remote sensing community [19]. However, most available attempts are based on an initial clustering, using spectral information alone, followed by a post-classification step using spatial context [20]. This operation entirely separates spatial information from spectral information, and thus the two types of information are not treated simultaneously.

In previous papers [21–24], we have explored the application of mathematical morphology operations to integrate both spatial and spectral responses in hyperspectral data analysis. Mathematical morphology is a classic nonlinear image processing technique that has been successfully applied to the processing of remotely sensed imagery [25,26].

Based on the set theory, binary morphology was established by introducing fundamental operators applied to two sets [27]. One set is processed by another one having a carefully selected shape and size, and known as the structuring element (SE), which is translated over the image. The SE acts as a probe for extracting or suppressing specific structures of the image objects, checking that each position of the SE fits within the image objects. Morphological operations have extended to gray-tone (mono-channel) images by viewing these data as an imaginary topographic relief; in this regard, the brighter the gray tone, the higher the corresponding elevation [28,29]. It follows that, in grayscale morphology, each 2-D gray tone image is viewed as if it were a digital elevation model (DEM). In practice, set operators directly generalize to gray-tone images. For instance, the intersection  $\cap$  (respectively, union  $\cup$ ) of two sets becomes the point-wise minimum  $\wedge$  (respectively, maximum) operator [30]. In a similar way to the binary case, specific image structures are extracted/suppressed according to the chosen SE. The latter is usually “flat” in the sense that it is defined in the spatial domain of the image (the  $x$ - $y$  plane) [25]. Therefore, classic mathematical morphology looks for objects defined as a specific spatial arrangement of image pixels rather than single pixels with a specific spectral signature.

The extension of the concepts of binary and grayscale morphology to multi/hyperspectral images is not straightforward. When such techniques are applied independently to each image channel (marginal morphology), there is a possibility for loss or corruption of information of the image due to the probability that new spectral constituents—not present in the original image—may be created as a result of processing image channels separately [31]. An alternative way to approach the problem of multi/hyperspectral morphology is to treat the data at each pixel as a vector. In order to define the basic morphological operations, a concept for a maximum (or minimum) is necessary, and thus it is important to define an appropriate arrangement of vectors in the selected vector space. A number of vector ordering schemes has been proposed, since there is no natural means of defining arrangement in  $N$ -D spaces. Several approaches have been suggested [32–34]: (1) in reduced ordering, a scalar parameter function is computed for each pixel of the image and the ordering is performed according to the resulting scalar values; (2) in partial ordering, the input multivariate samples are partitioned into smaller groups which are then ordered; (3) in conditional ordering the vectors are initially ordered according to the ordered values of their components, e.g. the first component. At the second step, vectors that have the same value for the first component are ordered according to the ordered values of another component, e.g. the second component, and so on. Our approach to this problem has been the definition of scalar vector ordering schemes based on the spectral purity of pixels [23]. First, a lattice structure is imposed onto  $N$ -D space by the definition of a cumulative distance measure. Second, morphological operations are defined by extension. By means

of extended morphological operations, a method for mixed pixel analysis of hyperspectral data was developed [21].

The main contribution of this paper with regard to our previous work in Refs. [21–23] is the development of an adaptative scheme that allows an intelligent and automated selection of the most appropriate SE to accurately characterize each pixel of the scene in both spatial and spectral terms. Some limitations of extended morphological operations were identified in Ref. [21] as a consequence of the fact that a fixed range of SE sizes was considered for every image pixel. The limitations above are solved in this paper by using the concept of morphological profile, defined in Ref. [35] for grayscale imagery. Conceptually, a grayscale morphological profile can be interpreted as a representation of the different output values, produced by a morphological operation at a certain image pixel, when the SE size is progressively increased from a minimum size to a maximum size. When extended to hyperspectral imagery, this concept allows for the selection of an optimum range of SE sizes at each pixel, thus improving its spatial/spectral characterization. A further contribution of this paper with regard to Ref. [24] is the construction of extended morphological transformations based on line segment SEs, which are able to accurately model oriented image features in complex analysis scenarios.

The remainder of the paper is organized as follows. Section 2 describes the approach followed for extension of classic morphological operations to hyperspectral imagery. In Section 3, a framework for the calculation of morphological profiles in hyperspectral data is described, and a number of examples is provided. Section 4 presents a comparison of the proposed analysis approach to other well-known full and mixed pixel classification approaches using both simulated and real data. Finally, conclusions and comments on plausible future research are stated in Section 5.

## 2. Extended morphological operations

Our attention in this section focuses primarily on the development of a mechanism to extend basic morphological operations to hyperspectral image data. The two basic operations of classic mathematical morphology are dilation and erosion. Following a usual notation [36], let us consider a grayscale image  $f$ , defined on a space  $E$ . Typically,  $E$  is the 2-D continuous space  $R^2$  or the 2-D discrete space  $Z^2$ . In the following, we refer to morphological operations defined on the discrete space. The flat erosion of  $f$  by  $B \subset Z^2$  is defined by the following expression:

$$(f \otimes B)(x, y) = \bigwedge_{(s,t) \in Z^2(B)} f(x+s, y+t), \quad (x, y) \in Z^2, \quad (1)$$

where  $Z^2(B)$  denotes the set of discrete spatial coordinates associated to pixels lying within the neighborhood defined

by  $B$  and  $\wedge$  denotes the minimum. On the other hand, the flat dilation of  $f$  by  $B$  is defined by

$$(f \oplus B)(x, y) = \bigvee_{(s,t) \in Z^2(B)} f(x-s, y-t), \quad (x, y) \in Z^2, \quad (2)$$

where  $\bigvee$  denotes the maximum. Using the same notation above, the composition

$$(f \circ B)(x, y) = [(f \otimes B) \oplus B](x, y), \quad (x, y) \in Z^2 \quad (3)$$

yields a flat opening, an operator that is increasing, anti-extensive and idempotent [36]. On the other hand, the composition

$$(f \bullet B)(x, y) = [(f \oplus B) \otimes B](x, y), \quad (x, y) \in Z^2 \quad (4)$$

is called a flat closing, an operator that is increasing, extensive, and idempotent. A morphological operator is called a morphological filter if it is increasing and idempotent [36]. In order to extend the above basic morphological operations to hyperspectral images, let us now consider an image  $f$ , defined on the ( $N$ -D) continuous space, where  $N$  is the number of spectral channels. An ordering relation can be imposed in the set of pixels lying within a flat SE, denoted by  $B$ , by defining metrics that calculate the cumulative distance between one particular pixel  $f(x, y)$ , where  $f(x, y)$  denotes an  $N$ -D vector at discrete spatial coordinates  $(x, y) \in Z^2$ , and every other pixel in the neighborhood given by  $B$ . Based on the previous considerations, flat extended dilation and flat extended erosion can be, respectively, defined as follows:

$$\begin{aligned} (f \oplus B)(x, y) &= \arg \left\{ \bigvee_{(s,t) \in Z^2(B)} \left[ \sum_s \sum_t \text{Dist}(f(x, y), \right. \right. \\ &\quad \left. \left. f(x+s, y+t) \right) \right] \right\}, \quad (x, y) \in Z^2, \quad (5) \end{aligned}$$

$$\begin{aligned} (f \otimes B)(x, y) &= \arg \left\{ \bigwedge_{(s,t) \in Z^2(B)} \left[ \sum_s \sum_t \text{Dist}(f(x, y), \right. \right. \\ &\quad \left. \left. f(x-s, y-t) \right) \right] \right\}, \quad (x, y) \in Z^2, \quad (6) \end{aligned}$$

where  $\text{Dist}$  is a point-wise distance measure between two  $N$ -D vectors. The choice of  $\text{Dist}$  is a key topic in the resulting ordering relation. This study has been presented in previous papers [21–23]. In this paper,  $\text{Dist}$  refers to the spectral angle distance (SAD), one of the standard metrics in hyperspectral analysis. Our choice of SAD is mainly based on the fact that this distance is invariant to multiplicative scaling that may arise due to different illumination conditions and sensor observation angle [10]. It should be noted

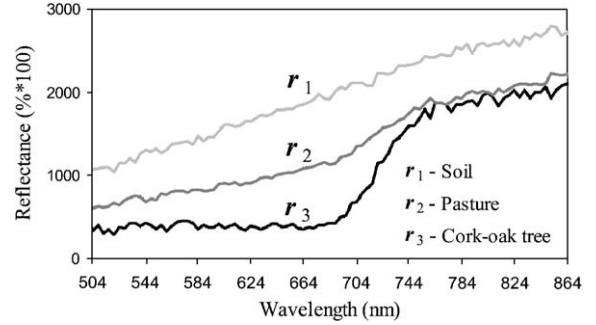


Fig. 1. Representative spectral signatures for the main constituents present in the original ROSIS hyperspectral image: soil ( $r_1$ ), pasture ( $r_2$ ) and cork-oak tree ( $r_3$ ).

that the  $\arg$  operator in Eqs. (5) and (6), respectively, selects the  $N$ -D pixel vector that maximizes and minimizes the cumulative distance value between  $f(x, y)$  and its neighboring pixels according to  $B$ . Hence, the use of SAD as the standard distance metric allows us to impose a partial order relationship of the vectors within a SE in terms of their spectral purity. We believe that a topic of great interest for future developments of the method is the detailed analysis of other distance measures that may be suitable for extension of morphological operations, including nonlinear distances as well as distances that use second-order statistics. It is important to notice that, regardless of the distance measure used, the proposed operators are vector preserving, i.e. no vector (constituent) that is not present in the input data is generated as a result of the extension process [22].

For illustrative purposes, let  $B$  be a flat  $3 \times 3$ -pixel SE and let  $f$  be a hyperspectral scene, collected by the DLR ROSIS imaging spectrometer (ROSIS—reflective optics system imaging spectrometers) [37] over a so-called ‘Dehesa’ ecosystem, mainly formed by cork-oak trees, soil and pasture, in Caceres, SW Spain. Representative spectral signatures of cork-oak trees, pasture and soil, selected from the above data set, are shown in Fig. 1 for illustrative purposes. The full hyperspectral scene consists of  $88 \times 134$  pixels of  $1.2 \times 1.2$  m, each containing 92 spectral bands covering the spectral range from 0.4 to 0.9  $\mu\text{m}$ . If  $B$  is moved pixel by pixel through  $f$ , then the SE defines a local spatial search area around each hyperspectral pixel. The result of applying an extended erosion/dilation operation to  $f$  using  $B$  is a new data cube, with exactly the same dimensions as the original, where each pixel has been replaced by the maximum/minimum of the neighborhood defined by the flat SE. The maximum (dilation) and minimum (erosion) pixel in the searched area is calculated according to the schema described above, yielding the results depicted in Fig. 2 for the spectral band collected at 584 nm wavelength by the ROSIS imaging spectrometer (see Fig. 2(a)). As can be examined in Fig. 2(b), extended dilation has the effect of expanding zones with ‘pure’ spectral signatures (in the

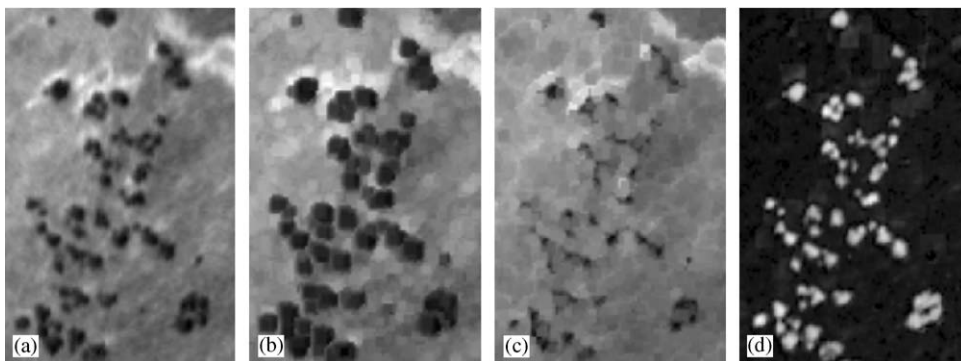


Fig. 2. (a) Band at 583.6 nm of original ROSIS hyperspectral image; (b) band at 583.6 nm of the hyperspectral image obtained after applying an extended erosion to the original image using a flat  $3 \times 3$  structuring element; (c) band at 583.6 nm of the hyperspectral image obtained after applying an extended dilation to the original image using a flat  $3 \times 3$  structuring element; (d) residual image obtained after applying an extended top-hat transformation to the original image using a flat  $7 \times 7$  structuring element.

example, cork-oak and soil areas are developed). Most of the pasture areas in the ROSIS scene are made up of soil mixtures and pasture because of the early growth stage of pasture at the time of sensor data acquisition (July 2001). This effect can be noticed in Fig. 2(c), where the erosion operation expands gray-tone (“mixed”) areas and shrinks both dark (cork-oak) and bright (pure soil) areas. With the two previous operations, the construction of extended flat opening and closing operations is straightforward (see Eqs. (3) and (4)). The proposed extended transforms can be used to isolate pure (opening) and mixed (closing) pixels in hyperspectral images, where the notion of pure/mixed refers to the most highly pure/mixed pixels among the surrounding pixels. In order to detect pure pixels, we define the extended top-hat operator,  $\Gamma$ , which is calculated by taking the residual image between the original and the opened image [38].

$$\Gamma[f(x, y)] = \text{Dist}[f(x, y), (f \circ B)(x, y)], \quad (x, y) \in Z^2. \quad (7)$$

For illustrative purposes, Fig. 2(d) shows the residual image obtained after applying an extended top-hat transformation to the original hyperspectral scene using a flat  $7 \times 7$  SE. In a similar way, the inverse extended top-hat operator,  $\Gamma'$ , can carry out the detection of mixed pixels in hyperspectral imagery.

$$\Gamma'[f(x, y)] = \text{Dist}[(f \bullet B)(x, y), f(x, y)], \quad (x, y) \in Z^2. \quad (8)$$

### 3. Extended morphological profiles

Our main goal in this section is to incorporate the idea of multi-scale analysis into extended morphological transformations. As described in Section 2, morphological filters are characterized by the size and shape of the considered SE. However, if the searched patterns do not have regular

properties across the scene, an adaptative scheme is needed to ensure that the correct SE size is considered at each pixel [39]. This need consequently poses the problem of adequate parameter selection. As reported by Pesaresi and Benediktsson, this selection can be achieved by plotting the morphological filter output at each pixel against the value of a varying parameter. The resulting plot is called a morphological profile, where the varying parameter is the size of the SE. Simple derivative rules can be applied to morphological profiles in order to determine the most appropriate parameter value for each pixel [35]. Morphological profiles in grayscale imagery are based on opening and closing by reconstruction [40], a special class of morphological filters that have proven to be very successful for multi-scale image processing. These filters do not introduce discontinuities, and therefore preserve the shapes observed in input images. Thus, the basic contrast imposed by conventional opening and closing versus reconstruction-based opening and closing, can be described as follows: conventional opening and closing remove the parts of the objects that are smaller than the SE, whereas opening and closing by reconstruction either completely removes the features or retains them as a whole. In Section 3.1, we detail the process followed to extend the concepts of opening and closing by reconstruction, morphological profiles, and derivative analysis to hyperspectral data. In Section 3.2, some illustrative examples are included. Finally, Section 3.3 describes a new methodology for mixed pixel classification, based on extended morphological profiles. The general algorithm, input parameters, and implementation options are also discussed.

#### 3.1. Construction of extended morphological profiles

In order to extend reconstruction-based opening and closing operations to hyperspectral imagery, let us consider a hyperspectral image  $f$  defined on  $R^N$ . Given a SE (designed

by  $B$ ) of minimal size, extended opening by reconstruction is defined by

$$(\mathbf{f} \circ B)^k(x, y) = \bigvee_{k \geq 1} [\delta_B^k(\mathbf{f} \circ B | \mathbf{f})](x, y), \quad (9)$$

where

$$[\delta_B^k(\mathbf{f} \circ B | \mathbf{f})](x, y) = \left[ \overbrace{\delta_B \delta_B \cdots \delta_B}^{k \text{ times}} (\mathbf{f} \circ B | \mathbf{f}) \right] (x, y). \quad (10)$$

The elementary term  $[\delta_B(\mathbf{f} \circ B | \mathbf{f})](x, y)$  is an extended geodesic dilation [41], defined as the maximum of the elementary dilation of  $\mathbf{f} \circ B$  using  $B$  at pixel  $(x, y)$  and the value of  $\mathbf{f}(x, y)$ ,

$$[\delta_B(\mathbf{f} \circ B | \mathbf{f})](x, y) = \{[(\mathbf{f} \circ B) \oplus B](x, y)\} \vee \{\mathbf{f}(x, y)\}. \quad (11)$$

As shown in Eq. (10), this operation is repeated  $k$  times until idempotence is reached. In a similar fashion, extended closing by reconstruction is given by

$$(\mathbf{f} \bullet B)^k(x, y) = \bigwedge_{k \geq 1} [\varepsilon_B^k(\mathbf{f} \bullet B | \mathbf{f})](x, y), \quad (12)$$

where

$$[\varepsilon_B^k(\mathbf{f} \bullet B | \mathbf{f})](x, y) = \left[ \overbrace{\varepsilon_B \varepsilon_B \cdots \varepsilon_B}^{k \text{ times}} (\mathbf{f} \bullet B | \mathbf{f}) \right] (x, y). \quad (13)$$

The elementary term  $[\varepsilon_B(\mathbf{f} \bullet B | \mathbf{f})](x, y)$  is an extended geodesic erosion [41], defined as the minimum of the elementary erosion of  $\mathbf{f} \bullet B$  using  $B$  at pixel  $(x, y)$  and the value of  $\mathbf{f}(x, y)$ ,

$$[\varepsilon_B(\mathbf{f} \bullet B | \mathbf{f})](x, y) = \{[(\mathbf{f} \bullet B) \otimes B](x, y)\} \wedge \{\mathbf{f}(x, y)\}. \quad (14)$$

Using Eqs. (10) and (13), extended morphological profiles are created as follows. Let the vector  $\mathbf{p}_k^\circ(x, y)$  be the extended opening by reconstruction profile at the point  $(x, y)$  of the image  $\mathbf{f}$ , defined by

$$\mathbf{p}_k^\circ(x, y) = \{(\mathbf{f} \circ B)^\lambda(x, y)\}, \quad \lambda = \{0, 1, \dots, k\} \quad (15)$$

and let  $\mathbf{p}_k^\bullet(x, y)$  be the extended closing by reconstruction profile at the point  $(x, y)$  of the image  $\mathbf{f}$ , defined by

$$\mathbf{p}_k^\bullet(x, y) = \{(\mathbf{f} \bullet B)^\lambda(x, y)\}, \quad \lambda = \{0, 1, \dots, k\}. \quad (16)$$

Here  $(\mathbf{f} \bullet B)^0(x, y) = \mathbf{f}(x, y) = (\mathbf{f} \circ B)^0(x, y)$  for  $\lambda = 0$  by the definition of extended opening and closing by reconstruction [40]. We define the derivative of the extended opening profile  $\Delta \mathbf{p}_k^\circ(x, y)$  as the vector

$$\Delta \mathbf{p}_k^\circ(x, y) = \{\text{Dist}[(\mathbf{f} \circ B)^\lambda(x, y), (\mathbf{f} \circ B)^{\lambda-1}(x, y)]\}, \quad \lambda = \{1, 2, \dots, k\}. \quad (17)$$

By duality, the derivative of the closing profile  $\Delta \mathbf{p}_k^\bullet(x, y)$  is the vector

$$\Delta \mathbf{p}_k^\bullet(x, y) = \{\text{Dist}[(\mathbf{f} \bullet B)^\lambda(x, y), (\mathbf{f} \bullet B)^{\lambda-1}(x, y)]\}, \quad \lambda = \{1, 2, \dots, k\}. \quad (18)$$

Given all of the above, the multi-scale opening characteristic  $\Phi_k^\circ(x, y)$  at the point  $(x, y)$  of the image  $\mathbf{f}$  is defined as the SE size with the greatest associated value in  $\Delta \mathbf{p}_k^\circ(x, y)$ ;

$$\Phi_k^\circ(x, y) = \lambda \in \{1, 2, \dots, k\}, \quad \text{Dist}[(\mathbf{f} \circ B)^\lambda(x, y), (\mathbf{f} \circ B)^{\lambda-1}(x, y)] = \bigvee \Delta \mathbf{p}_k^\circ(x, y). \quad (19)$$

Similarly, the multi-scale closing characteristic  $\Phi_k^\bullet(x, y)$  is defined as the SE size with the greatest associated value in the derivative of the extended closing profile  $\Delta \mathbf{p}_k^\bullet(x, y)$ ;

$$\Phi_k^\bullet(x, y) = \lambda \in \{1, 2, \dots, k\}, \quad \text{Dist}[(\mathbf{f} \bullet B)^\lambda(x, y), (\mathbf{f} \bullet B)^{\lambda-1}(x, y)] = \bigvee \Delta \mathbf{p}_k^\bullet(x, y). \quad (20)$$

### 3.2. Examples

This section provides some examples illustrating the construction of extended morphological profiles, derivatives and multi-scale characteristics. In Fig. 3, the procedure followed in Section 3.1 to obtain extended morphological profiles is illustrated by using four target objects in a ROSIS hyperspectral image: a small cork-oak tree (see Fig. 3(a)), a pure soil area (Fig. 3(b)), a medium-sized cork-oak tree (Fig. 3(c)), and a mixed area formed by soil and pasture, surrounded by pure soil (Fig. 3(d)). Ground-truth information, collected during a site visit to the area, was used to characterize the spectral purity of sample pixels associated to these objects. As part of our experiment, the data from this site visit were compiled as a collection of spectral measurements with accurate geo-registration. Data collection revealed that, while the pixels in Figs. 3(a)–(c) can be considered spectrally pure, the relatively high spatial resolution available was not large enough to separate soil from pasture at the pixel shown in Fig. 3(d). As a result, this pixel was labeled as spectrally mixed.

Extended morphological profiles were constructed for the pixels shown in Fig. 3. The resulting opening  $\mathbf{p}_k^\circ(x, y)$  and closing  $\mathbf{p}_k^\bullet(x, y)$  profiles (see Eqs. (15) and (16)) were combined in 3-D plots, where the spectral signature of the analyzed pixel  $\mathbf{f}(x, y)$ , denoted by  $P$  in the plots, is shown along with the resulting spectral signatures obtained after applying a series of opening- and closing-by-reconstruction operations using different SE sizes. A range of SEs was considered in experiments. The range was derived by being based on three iterations of the elementary eight-connected

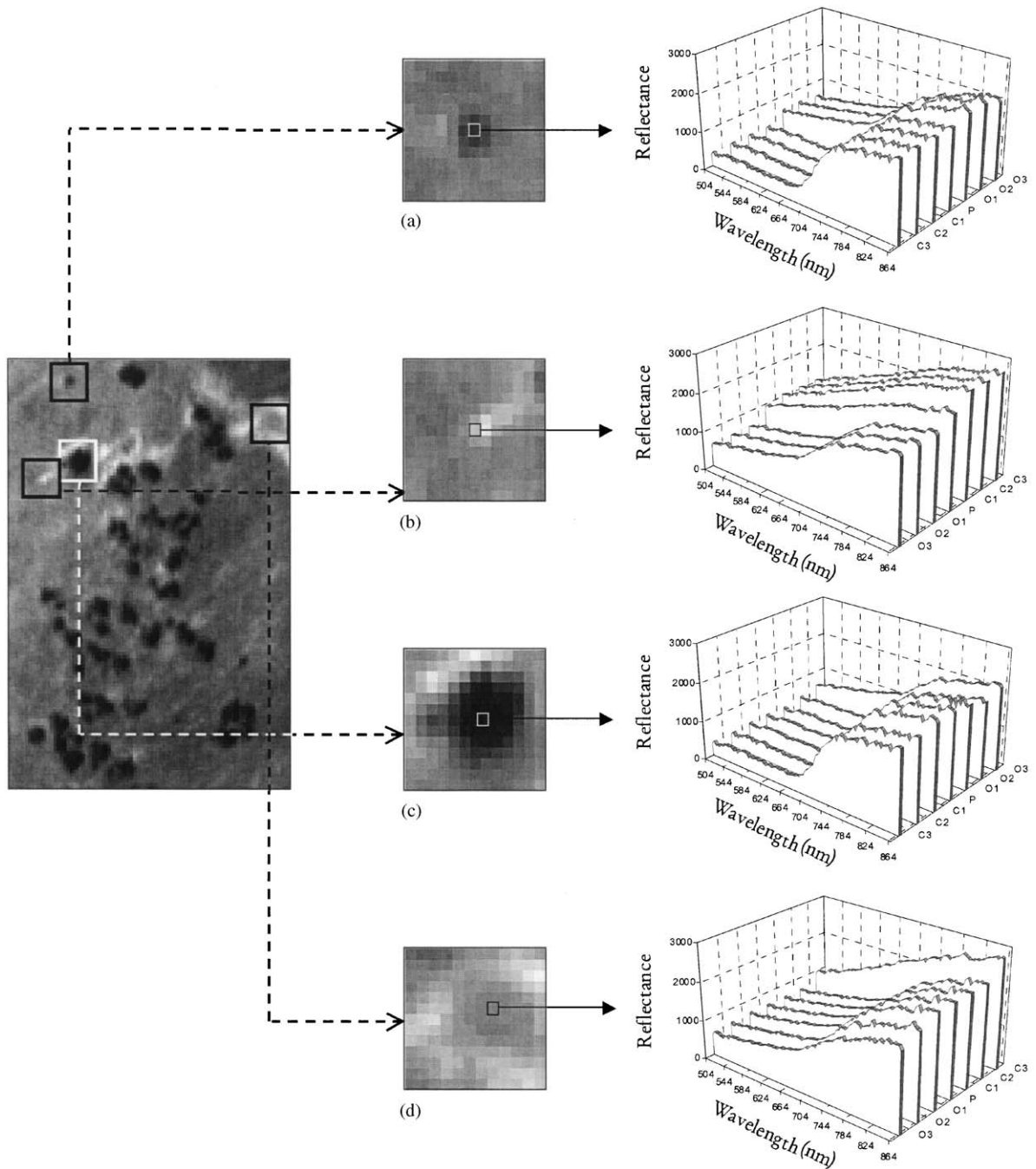


Fig. 3. Extended morphological profiles associated to pixels belonging to four target objects in a ROSIS hyperspectral scene: (a) small cork-oak tree; (b) pure soil area; (c) medium-sized cork-oak tree; (d) mixed area formed by soil and pasture, surrounded by pure soil.

SE (using Eqs. (10) and (13), respectively). These iterations were labeled in the plots as  $Ok = (f \circ B)^k(x, y)$  for the opening series, and  $Ck = (f \bullet B)^k(x, y)$  for the closing series, where  $k = \{1, 2, 3\}$ . As it can be observed in

Figs. 3(a)–(c), pure pixels remain indifferent to the three closing-by-reconstruction iterations, but are replaced during the opening-by-reconstruction process. Similarly, it is shown in Fig. 3(d) that the mixed pixel remains indifferent to the

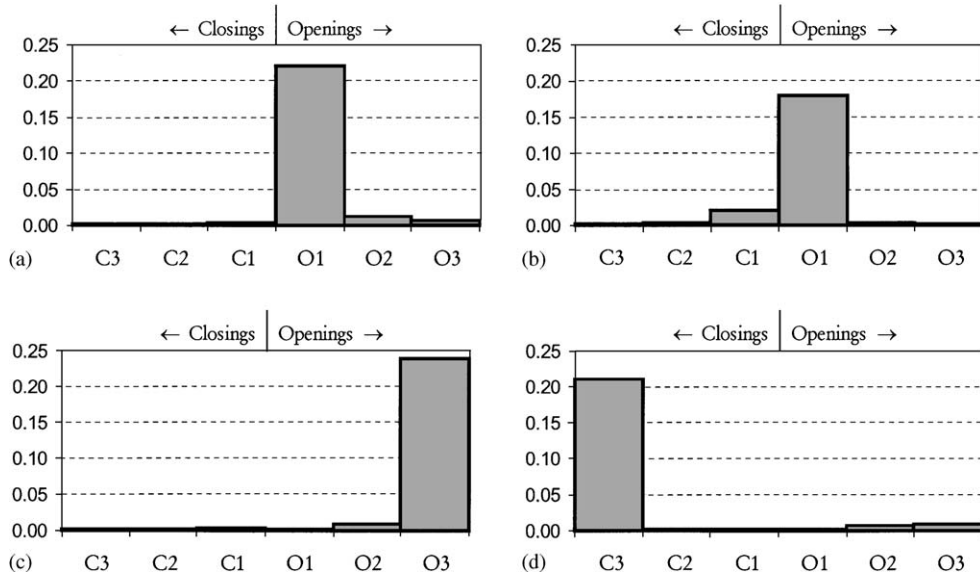


Fig. 4. Derivatives of the morphological profiles associated with target pixels in: (a) small cork-oak tree; (b) pure soil area; (c) medium-sized cork-oak tree; (d) mixed area formed by soil and pasture, surrounded by pure soil.

three opening-by-reconstruction iterations, but is replaced in the closing series. The step of the opening/closing series iteration at which the pixel is replaced provides an intuitive idea of both the spectral purity of the pixel and the spatial distribution of the object in the scene.

Fig. 4 shows graphs where the resulting opening and closing derivative profiles for each analyzed pixel in Fig. 3 are combined in single 2-D plots. These plots can be interpreted as histograms that show the level of the derivative relative to the opening and closing series for each step of the iteration (see Eqs. (17) and (18)). We emphasize that the behavior of the derivative profile stores information about the spectral and spatial characteristics of the pixel in relation to its neighboring pixels. As a result, pixels that are spectrally purer than their adjacent components have a combined derivative profile that is unbalanced to the right (opening series), as shown in Figs. 4(a)–(c). In contrast, mixed pixels show a derivative profile that is unbalanced to the left (closing series), as illustrated in Fig. 4(d). The point where the derivative profile takes the maximum value can be used to record the most appropriate size of the SE for each pixel. This value provides an indication of the morphological characteristic of a certain spectral feature in the given spatial domain range, which can be used to evaluate the purity of the pixel using a spatial/spectral criterion.

### 3.3. Proposed algorithm

As explained in Section 2, the residual images lying between extended opening-by-reconstruction (or extended closing-by-reconstruction) images and the original hy-

Table 1  
The ADMP algorithm

---

Inputs:  
 Hyperspectral pixel vector:  $f(x, y)$ .  
 Maximum number of iterations:  $k$ .

Outputs:  
 $f(x, y)$  labeled as “pure” or “mixed”.  
 Morphological profile purity index,  $\Pi(x, y)$ , at  $f(x, y)$ .

Begin  
 $p_k^\circ(x, y) = \{(f \circ B)^\lambda(x, y)\}$ ,  $\lambda = \{0, 1, \dots, k\}$ ,  
 $p_k^\bullet(x, y) = \{(f \bullet B)^\lambda(x, y)\}$ ,  $\lambda = \{0, 1, \dots, k\}$ .  
 If  $\sqrt{\Delta p_k^\circ(x, y)} > \sqrt{\Delta p_k^\bullet(x, y)}$  then  
 label  $f(x, y)$  as “pure”.  
 $\Pi(x, y) = \text{Dist}[f(x, y), (f \circ B)^{\lambda^\circ}(x, y)]$ ,  
 where  $\lambda^\circ = \Phi_k^\circ(x, y)$ .  
 Else  
 label  $f(x, y)$  as “mixed”.  
 $\Pi(x, y) = \text{Dist}[f(x, y), (f \bullet B)^{\lambda^\bullet}(x, y)]$ , where  $\lambda^\bullet = \Phi_k^\bullet(x, y)$ .  
 Endif  
 End

---

perspectal image can be interpreted as a measure of the relative pure (mixed) condition of the pixel compared to its neighbors. With this result in mind, a novel multi-scale algorithm is described for the determination of a morphological profile-based purity index, denoted by  $\Pi(x, y)$ , at each pixel  $f(x, y)$  of a hyperspectral image. This algorithm is abbreviated from now on as automated determination of morphological profiles (ADMP).

The ADMP algorithm is addressed in Table 1. Taking into account the reasoning illustrated in Section 3.2, we

can summarize the underlying ideas governing ADMP as follows. Firstly, those pixels that remain indifferent to the closing-by-reconstruction process but are replaced during opening by reconstruction can be designed as “pure”. In contrast, those pixels that remain indifferent to the opening-by-reconstruction process but are replaced during closing by reconstruction can be labeled as “mixed”. Hence, pure/mixed pixels can be easily identified by comparing the maximum derivative value obtained in the opening-by-reconstruction series, i.e.  $\sqrt{\Delta p_k^{\circ}(x, y)}$ , to the maximum derivative value produced by the closing-by-reconstruction series, i.e.  $\sqrt{\Delta p_k^{\bullet}(x, y)}$ . As shown in Table 1, if  $f(x, y)$  is labeled as “pure”, then its associated purity index  $\Pi(x, y)$  is calculated as the residual between the extended opening-by-reconstruction and the original pixel. In contrast, if  $f(x, y)$  is designed as a mixed pixel by ADMP, then  $\Pi(x, y)$  is calculated as the residual between the extended closing-by-reconstruction and the original pixel. In both cases, the operation is performed by using an optimum SE size, provided by  $\Phi_k^{\circ}(x, y)$  and  $\Phi_k^{\bullet}(x, y)$ , respectively (see Eqs. (19) and (20)). It should be noted that the algorithm described in Table 1 is characterized by a simple behavior, where both the opening and closing profiles have only one significant derivative maximum. This assumption may not be valid in complex image scenes characterized by structures with several significant derivative maxima and directional features (for instance, urban environments). In the above cases, orientation is a worthy addition to scale information in order to characterize image structures [24,42]. In the following, we propose an extension of the procedure used to calculate  $\Pi(x, y)$  that makes use of both scale and orientation information.

Scale-orientation morphological profiles can be simply created, using the same definitions given in Section 3.1, by considering SEs given by a certain size and orientation [24]. Let us denote by  $B_{(dx, dy)}$  a line segment SE (LSSE) of minimal length, where  $dy/dx$  is the slope of the line segment [42]. Since we are dealing with images digitized on a square grid, we can restrict our analysis to line slopes in the form of an irreducible fraction  $dy/dx$  (i.e.  $dx$  and  $dy$  are integers with no common divisors). By convention, it is convenient to include the forms  $0/1$  and  $1/0$  for referring to horizontal and vertical lines, respectively. For example, Figs. 5(a)–(d) shows four LSSEs of length equal to three pixels for a slope of  $0/1$ :  $B_{(0,1)}$  (Fig. 5(a)),  $1/0$ :  $B_{(0,1)}$  (Fig. 5(b)),  $1/-1$ :  $B_{(1,-1)}$  (Fig. 5(c)), and  $-1/1$ :  $B_{(-1,1)}$  (Fig. 5(d)). As shown in Figs. 5(e)–(h), LSSEs of increased length and width can be obtained by applying binary dilation operations, using a square-shaped  $3 \times 3$ -pixel SE, to the above LSSEs of minimal length. If we consider the SAD distance as the basis for constructing extended morphological profiles using LSSEs (see Section 3.1), we can define the orientation at a given hyperspectral image pixel  $f(x, y)$  as the orientation of the LSSE that maximizes the SAD between the spectral signature in the original image at the point  $(x, y)$  and the spectral signature at the same location in the image filtered by the

considered LSSE. As a result, directional openings produce a high response with image structures that occur in the direction of the considered LSSE and, at the same time, are spectrally purer than their background. On the other hand, directional closings are appropriate to detect image structures in the direction of the considered LSSE, which are less spectrally pure (i.e. “more highly mixed”) than their background [24]. It should be noted that, for pixels belonging to wide (with respect to the LSSE) objects of similar spectral properties, several distinct orientations may output the maximum SAD distance value. In the above situation, a LSSE of increased length and width is required to characterize the object.

Using the above concepts, we have modified the ADMP algorithm in Table 1 to incorporate information about the orientation at each analyzed hyperspectral image pixel  $f(x, y)$ . The extended algorithm, abbreviated from now on as automated determination of scale-orientation morphological profiles (ADSOMP), works as follows (see Table 2): For each  $f(x, y)$ , a set of LSSEs at different orientations are applied to construct extended opening- and closing-by-reconstruction morphological profiles with scale-orientation information. The range of orientations explored in this work is limited to four orientations, although additional orientations can be easily incorporated in future developments of the method. For each orientation, a directional opening-  $[p_{k,(dx,dy)}^{\circ}(x, y)]$  and closing-by-reconstruction  $[p_{k,(dx,dy)}^{\bullet}(x, y)]$  morphological profile is obtained by applying a directional LSSE designed by  $B_{(dx,dy)}$ . A collection of derivative maxima (one per each considered orientation) is then calculated, and the resulting information is used to label the original pixel as “pure” or “mixed”. If  $f(x, y)$  is labeled as “pure” by the modified algorithm, then its associated purity index  $\Pi(x, y)$  is calculated as the residual between the original pixel and the result of an extended directional opening-by-reconstruction operation. In contrast, if  $f(x, y)$  is designed as a mixed pixel, then  $\Pi(x, y)$  is calculated as the residual between the original pixel and the result of an extended directional closing-by-reconstruction operation. In either case, the operation is performed by using the LSSE that provides a higher response at the range of scales and orientations explored, i.e.  $\Phi_{k,(dx,dy)}^{\circ}(x, y)$  or  $\Phi_{k,(dx,dy)}^{\bullet}(x, y)$ , respectively.

In this work, we mainly use the ADMP and ADSOMP algorithms for the relevant task of selecting a suitable set of candidate endmembers for spectral mixture analysis of hyperspectral image scenes. A general block diagram of the proposed method is depicted in Fig. 6. The resulting method is an extension of our previous approach, automated morphological endmember extraction (AMEE), which is based on two parameters,  $S_{\min}$  and  $S_{\max}$ , that, respectively, denote the minimum and maximum SE sizes considered in an iterative process of combined erosion/dilation operations [21]. The size of these parameters is the same at each iteration for all the pixels of the scene. In the proposed adaptive

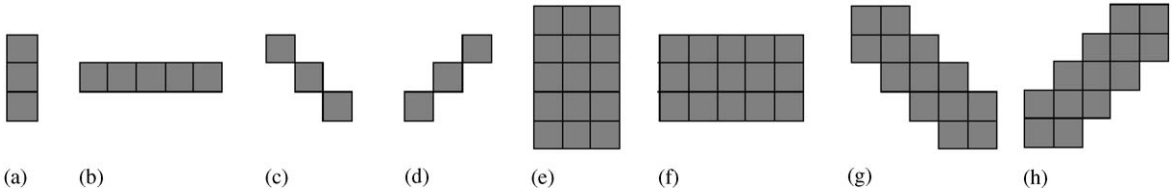


Fig. 5. Line segment structuring elements (LSSEs) of minimal length (3 pixels) at four different orientations (a)–(d). LSSEs of increased length and width at four different orientations (e)–(h), obtained by applying binary dilation operations to (a)–(d), using a square-shaped 3 × 3-pixel structuring element.

Table 2  
The ADSOMP algorithm

---

Inputs:  
 Hyperspectral pixel vector:  $f(x, y)$ .  
 Maximum number of iterations:  $k$ .

Outputs:  
 $f(x, y)$  labeled as “pure” or “mixed”.  
 Morphological profile purity index,  $\Pi(x, y)$ , at  $f(x, y)$ .

Begin  
 For each  $(dx, dy) = [(0, 1), (1, 0), (1, -1), (-1, 1)]$  do begin  
 $p_{k,(dx,dy)}^{\circ}(x, y) = \{[f \circ B_{(dx,dy)}]^{\lambda}(x, y)\}, \quad \lambda = \{0, 1, \dots, k\}$ .  
 $p_{k,(dx,dy)}^{\bullet}(x, y) = \{[f \bullet B_{(dx,dy)}]^{\lambda}(x, y)\}, \quad \lambda = \{0, 1, \dots, k\}$ .  
 Endfor  
 If  $\sqrt{\{\Delta p_{k,(dx,dy)}^{\circ}(x, y); (dx, dy) = [(0, 1), (1, 0), (1, -1), (-1, 1)]\}} > \sqrt{\{\Delta p_{k,(dx,dy)}^{\bullet}(x, y); (dx, dy) = [(0, 1), (1, 0), (1, -1), (-1, 1)]\}}$  then  
 label  $f(x, y)$  as “pure”.  
 $\Pi(x, y) = \sqrt{\{\text{Dist}[f(x, y), [f \circ B_{(dx,dy)}]^{\lambda^{\circ}}(x, y)]\}},$  where  $\lambda^{\circ} = \Phi_{k,(dx,dy)}^{\circ}(x, y)$  and  $(dx, dy) = [(0, 1), (1, 0), (1, -1), (-1, 1)]$ .  
 Else  
 label  $f(x, y)$  as “mixed”.  
 $\Pi(x, y) = \sqrt{\{\text{Dist}[f(x, y), [f \bullet B_{(dx,dy)}]^{\lambda^{\bullet}}(x, y)]\}},$  where  $\lambda^{\bullet} = \Phi_{k,(dx,dy)}^{\bullet}(x, y)$  and  $(dx, dy) = [(0, 1), (1, 0), (1, -1), (-1, 1)]$ .  
 Endif  
 End

---

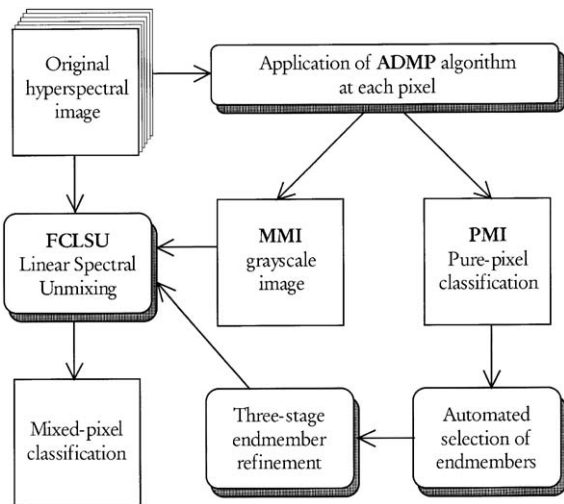


Fig. 6. Pseudo-code diagram of the proposed analysis method.

approach, the most appropriate SE for each pixel is automatically calculated by using extended morphological profiles. As Fig. 6 shows, the input to the method is the full hyperspectral data cube, with no previous dimensionality reduction. Firstly, either the ADMP or ADSOMP algorithm is applied to each pixel of the original image. As a result, two grayscale images are produced, called pure morphological image (PMI) and mixed morphological image (MMI). The PMI contains those pixels labeled as “pure” by the applied algorithm, while the MMI contains those pixels labeled as “mixed”. Each pixel position  $(x, y)$  in both PMI and MMI stores the associated  $\Pi(x, y)$  score calculated by ADMP or ADSOMP. Automated endmember selection is performed at the PMI by using a threshold value. Several techniques have been discussed in the literature for automated thresholding of grayscale images [43]. In our application, we have found appropriate results by using the multi-level Otsu method [44], an approach based on the minimization of the weighted sum of group variances. The final selection of endmembers is refined by a three-stage approach which consists of the following steps: (1) spatial/spectral region growth,

(2) calculation of mean spectra from resulting regions, and (3) redundant endmember thinning (see Ref. [23] for a more detailed discussion of these steps). As a result, a final set of endmembers is obtained. Mixed pixels, marked at the MMI, are now expressed in terms of linear combinations of extracted endmembers, producing a mixed pixel classification output. The above operation is achieved by a simple least squares inversion of the original hyperspectral image using Eq. (1) with abundance-sum-to-one and abundance-non-negativity constraints [15]. The inversion process, called fully constrained linear spectral unmixing (FCLSU), has demonstrated to provide accurate sub-pixel fractional cover estimation if (1) selected endmembers have been adequately chosen, and (2) the linear mixture model is flexible enough to accommodate the full range of spectral variability throughout the observed landscape.

#### 4. Experimental results

To assess the effectiveness of our novel approach to mixed pixel classification of hyperspectral imagery, different experiments were carried out on a data set made up of simulated and real data. In these experiments, the performance of the proposed analysis method will be assessed theoretically and compared against other standard full and mixed pixel classifiers, using a specifically designed quantitative framework.

##### 4.1. Experiments with simulated data

Our main goal in this section is to examine the accuracy of the proposed method in estimating abundance fractions from mixed pixels. This is a relevant task with straightforward applications in agriculture and farming. For example, in the southern parts of the Iberian Peninsula, Dehesa systems are traditionally used for a combination of livestock, forest and agriculture activity. The outputs of Dehesa systems include meat, milk, wool, charcoal, cork bark and grain. Around 12–18% of the area is harvested on a yearly basis. The crops are used for animal feed or for cash cropping, depending on the rainfall of the area. In such environment, determining the fractional abundance of materials allows for a better monitoring of natural resources. Unfortunately, accurate ground-truth information related to the fractional coverage of materials inside each pixel is very difficult to obtain in a real-world scenario [45]. As a result, mixed pixel analysis techniques are difficult to validate and substantiate. In order to overcome the above limitation, a commonly accepted approach in the literature has been the use of simulated imagery (see for example Refs. [46,47]). It should be taken into account that simulated scenes may not fully describe the complexity of a real landscape but, if carefully simulated, they have the advantage that the abundance fractions of constituents can be fully controlled and varied as necessary.

In our experiments, the proposed method was tested on a simulated hyperspectral scene representing a semi-vegetated



Fig. 7. Ground-truth data collection at a Dehesa test site in SW Spain by using an ASD FieldSpec Pro spectro-radiometer.

Dehesa landscape. The choice of this type of landscape for the simulation was made on two accounts: (1) its simplicity, and (2) the availability of ROSIS hyperspectral data for a real Dehesa test site in Caceres, SW Spain. Partial ground-truth is available for this site, given by the true spatial locations of pixels belonging to cork-oak trees. These objects were accurately geo-registered in the image by using GPS data collected during a visit to the test site. We have treated the simple Dehesa landscape as a surface covered by two dominant classes, namely background and cork-oak trees. Three spectral signatures, denoted from now on as  $r_1$  (soil),  $r_2$  (pasture), and  $r_3$  (cork-oak tree) were selected from available ROSIS data for computer simulations (see Fig. 1). Background was simulated by using  $r_1$  and  $r_2$  uniformly, with their respective abundance fractions being positive and summed to one. Cork-oak trees were simulated by using partial ground-truth related to target locations in the scene. As a result, the spatial distribution and pixel size of cork-oak trees in our simulated  $88 \times 134$  pixel scene accurately resembles the real characteristics of trees at the original scene (see Fig. 2(a)). A model was adopted for simulation of different levels of tree crown transparency, a phenomenon that was experimentally observed from ground measurements, collected at the top of tree crowns at the test site by using an ASD FieldSpec Pro spectro-radiometer (see Fig. 7). Based on these observations, cork-oak tree simulation was made based on two major assumptions: (1)  $r_3$  is assumed to be the predominant underlying material at simulated cork-oak mixed pixels, and (2) although  $r_1$  and  $r_2$  may also be present at these pixels, their combined fractional amount is below the assigned abundance fraction for  $r_3$ .

Random noise was added to the scene in order to simulate contributions from ambient (clutter) and instrumental sources. Noise was created by using numbers with a standard normal distribution obtained from a pseudorandom number generator and added to each pixel to generate a signal-to-noise ratio (SNR) of 30:1. For the simulations, we will consider each band SNR the ratio of the 50% signal

level to the standard deviation of the noise, following the definition given in Ref. [48]. This results in noise standard deviation that is roughly proportional to the average signal, a phenomenon that is often observed in radiometric data. Thus, the simulated hyperspectral data are created, based on a simple linear mixture model, by the following expression:

$$s(x, y) = \left( \frac{\text{SNR}}{2} + \mathbf{n}(x, y) \right) \cdot [\alpha_1(x, y) \cdot \mathbf{r}_1 + \alpha_2(x, y) \cdot \mathbf{r}_2 + \alpha_3(x, y) \cdot \mathbf{r}_3], \quad (21)$$

where  $s(x, y)$  denotes a vector containing the simulated discrete spectrum at the pixel with spatial coordinates  $(x, y)$  of the simulated image;  $\alpha_i(x, y)$ ,  $i = 1, \dots, 3$  is the assigned fractional abundance of spectral signature  $\mathbf{r}_j$  at the pixel, and  $\mathbf{n}(x, y)$  is the noise factor. Abundance-sum-to-one and abundance-non-negativity constraints are imposed in Eq. (21) in order to provide the simulation with adequate physical meaning [15]. Moreover, based on our model assumptions, two additional constraints, namely  $\alpha_3(x, y) = 0$  and  $\alpha_3(x, y) > 0.5$ , are imposed in the simulation of background and cork-oak tree pixels, respectively. It should be noted that, for simplicity, multiple scattering effects have not been simulated. In addition, we have assumed uniform illumination throughout the scene. Fig. 8 shows the fractional abundance maps assignment to the main constituents of our simulated scene, i.e.  $\mathbf{r}_1$  (see Fig. 8(a)),  $\mathbf{r}_2$  (Fig. 8(b)) and  $\mathbf{r}_3$  (Fig. 8(c)). These fractional maps will be used as ground-truth for the comparisons.

In order to perform abundance estimation simulations, we have applied the PPI, N-FINDR, AMEE and original ADMP-based mixed pixel classifiers to the simulated scene described in this section. Prior to a full examination and discussion of results, it is important that the parameter values used for PPI, AMEE and ADMP-based algorithms are described, bearing in mind that N-FINDR does not require any input parameters. In the PPI method, the value of the  $C$  parameter was set to the mean of PPI scores obtained after  $L = 10^4$  iterations, so that only pixels with a PPI score above the average were selected as endmember candidates. This approach has been previously suggested in order to obtain satisfactory results from the algorithm [49]. Pixels were then grouped into smaller subsets based on their clustering in the  $N$ -D space. Finally, resulting groups of extreme pixels were linked to the original image, and the mean spectrum of each group was used as a candidate endmember for unmixing [16]. The spatial domain probed in this experiment by the AMEE and ADMP-based methods was provided by a range of increasing square-shaped SEs with sizes ranging from  $3 \times 3$  pixels (3.6 m) up to  $7 \times 7$  pixels (8.4 m). This range was determined empirically after conducting a set of preliminary experiments with real ROSIS data (see Section 3.2). The above mixed pixel methods were used to obtain a set of endmembers associated with each constituent material of the simulated scene ( $\mathbf{r}_1$ ,  $\mathbf{r}_2$  and  $\mathbf{r}_3$ , respectively); the abundance of each endmember was estimated by us-

ing FCLSU linear spectral unmixing. We can visualize the performance of these methods by plotting estimated in contrast to true abundances for the different constituents at each image pixel. In Fig. 9, scatterplots of true versus estimated abundance values and resulting root mean square error (RMSE) are shown for each method and material. In general, we observe that acceptable quantitative agreements between the estimated and true abundances are obtained. In addition, the four methods tested are observed to produce low RMSE scores for  $\mathbf{r}_1$ ,  $\mathbf{r}_2$  and  $\mathbf{r}_3$ . However, we notice that both AMEE (see Figs. 9(g)–(i)) and ADMP-based (Figs. 9(j)–(l)) methods produce lower RMSE scores than PPI (Figs. 9(a)–(c)) and N-FINDR (Figs. 9(d)–(f)). This finding objectively confirms our insight: that the incorporation of spatial information improves mixed pixel classification by reducing algorithm sensitivity to noise and mixture complexity. In fact, a comparison of the results produced by AMEE and ADMP-based methods reveals that the adaptive approach introduced by ADMP in the selection of SEs results in a significant improvement in terms of abundance estimation over the simple multi-scale decomposition scheme performed by AMEE. The proposed method is able to accurately classify background pixels (formed by binary mixtures of  $\mathbf{r}_1$  and  $\mathbf{r}_2$ ) and cork-oak tree pixels (formed by ternary mixtures of  $\mathbf{r}_1$ ,  $\mathbf{r}_2$  and  $\mathbf{r}_3$ ) with sub-pixel precision. Nonetheless, it should be clarified that, because of the simple nature of the simulation carried out in this section, the above observations are not conclusive. In order to test these statements in a more complex situation, the development of further experiments using real hyperspectral data are highly pertinent.

#### 4.2. Experiments with real data

Two different experiments with real hyperspectral data sets are carried out in this section. The first experiment utilizes a portion of an AVIRIS imaging spectrometer data set taken over NW Indiana's Indian Pines agricultural test site in June 1992. This  $68 \times 86$ -pixel scene, available from David A. Landgrebe [50] is characterized by low spatial resolution (pixels of  $17 \times 17$  m, each of which contains 220 bands covering 400–2500 nm). In the second experiment, data from the DAIS 7915 airborne imaging spectrometer of DLR were used. The data were collected in July 2001 over the city of Pavia, Italy, with high ground resolution pixels of  $5 \times 5$  m, and size of  $400 \times 400$  pixels, each of which contains 72 spectral bands covering 496–2412 nm [51]. In both cases, there is ground-truth information available, expressed in the form of a class assignment for each labeled hyperspectral image pixel, with ground-truth classes being mutually exclusive.

Before describing the ground-truth data and experimental results, we should first note that, with no availability of ground-truth information about the contribution of underlying constituent materials at each pixel, a quantitative analysis for mixed pixel classification is not possible in the above scenes. In contrast, full pixel classification does not

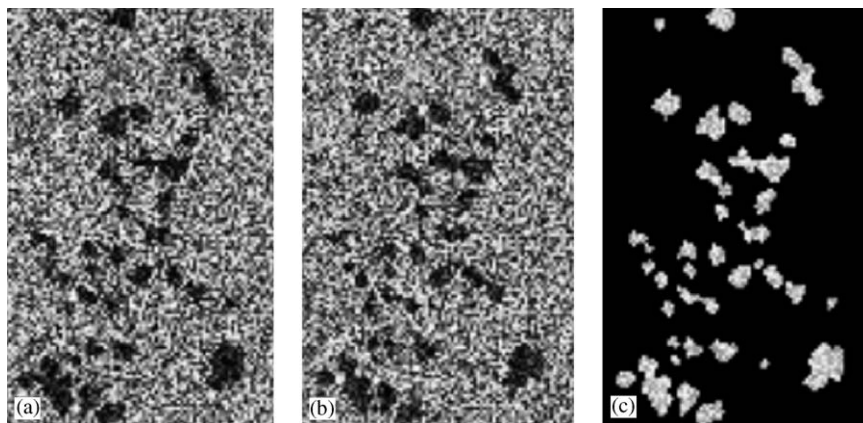


Fig. 8. Description of simulated Dehesa landscape scene: (a) abundance fractions assigned to  $r_1$ ; (b) abundance fractions assigned to  $r_2$ ; (c) abundance fractions assigned to  $r_3$ .

have such a problem. Unlike mixed pixel classification, it does not require abundance fractions of spectral signatures to be used for class assignment. Its performance is completely determined by the criteria used for classification. Hence, in order to carry out an experimental comparison among a set of mixed pixel classification algorithms using available ground-truth data, it is first necessary to establish a link between mixed pixel classification and full pixel classification. In order to achieve such a goal, we follow the approach proposed in Ref. [52], based on the definition of a mixed-to-pure (M/P) pixel converter. This approach interprets the mixed pixel classification problem in the context of pure pixel classification by using a linear mixture model. Let us assume that a mixed pixel classifier recognizes  $E$  pure signatures  $\{e_i\}_{i=1}^E$  in the scene, where  $e_j$  is the  $j$ th signature. Let  $s(x, y)$  be a mixed pixel to be classified, and let  $\hat{s}(x, y) = [\hat{\alpha}_1(x, y)\hat{\alpha}_2(x, y)\dots\hat{\alpha}_E(x, y)]^T$  be the estimated  $E$ -dimensional abundance vector, where  $\hat{\alpha}_j(x, y)$  is the estimated abundance fraction of material  $e_j$  in  $s(x, y)$ . A simple M/P converter for  $s(x, y)$  can be constructed by using the winner-take-all (WTA) thresholding criterion, an approach that is very similar to the WTA learning algorithm commonly applied in neural networks [53]. By using WTA, we can compare all estimated abundance fractions  $\{\hat{\alpha}_1(x, y), \hat{\alpha}_2(x, y), \dots, \hat{\alpha}_E(x, y)\}$  and find the one with the maximum fraction, say  $\hat{\alpha}_{j^*}(x, y)$ , by the following expression:

$$j^* = \arg \left\{ \max_{1 \leq j \leq E} \{\hat{\alpha}_j(x, y)\} \right\}. \quad (22)$$

The resulting fraction is used to classify  $s(x, y)$  by assigning it to a class given by the  $j^*$ th signature  $e_j$ . In other words, using the WTA criterion we can define an M/P converter by setting  $\hat{\alpha}_{j^*}(x, y) = 1$  and  $\hat{\alpha}_j(x, y) = 0$  for  $j \neq j^*$ . With the above assumptions in mind, we proceed to describe the classification results obtained after applying different

mixed pixel classifiers to the AVIRIS Indian Pines and DAIS 7915 Pavia data sets.

#### 4.2.1. Experiment with AVIRIS data comprising agricultural fields in Indian Pines, Indiana

The  $68 \times 86$ -pixel AVIRIS data set considered for experiments in this section is formed by about two-thirds of agricultural fields (corn and soybeans) and one third of grass. It should be noted that the SNR at the time of data acquisition was considerably lower than current AVIRIS standards [54]. There is ground truth for over 75% of the scene, comprised of four classes given by different agricultural fields: (1) corn-no till; (2) soybean-no till; (3) minimum-soybean (soybean min till); (4) grass. Ground-truth availability has made this scene a widely used test case for validation of hyperspectral analysis methods [55]. These classes have similar spectral signatures and are very difficult to discriminate. In addition, low spatial resolution results in high mixture complexity in most of the pixels, making the scene a challenging classification problem as reported by previous research [56]. The test data and the ground truth map are shown in Fig. 10, where the different regions have been labeled with the initial letter of the class name plus a number. As shown in Fig. 10, ground-truth is expressed in the form of a class assignment for each labeled hyperspectral image pixel, with ground-truth classes being mutually exclusive. The number of labeled pixels in each class is addressed in Table 3.

Before addressing the classification results obtained after applying PPI, N-FINDR, AMEE and ADMP-based mixed pixel classifiers to the Indian Pines AVIRIS dataset, it is important to outline parameter values used for the different methods, bearing in mind that the N-FINDR method does not require any input parameters. Parameter values used for PPI are the same as those used in experiments with simulated data [49]. In contrast, the spatial domain explored in

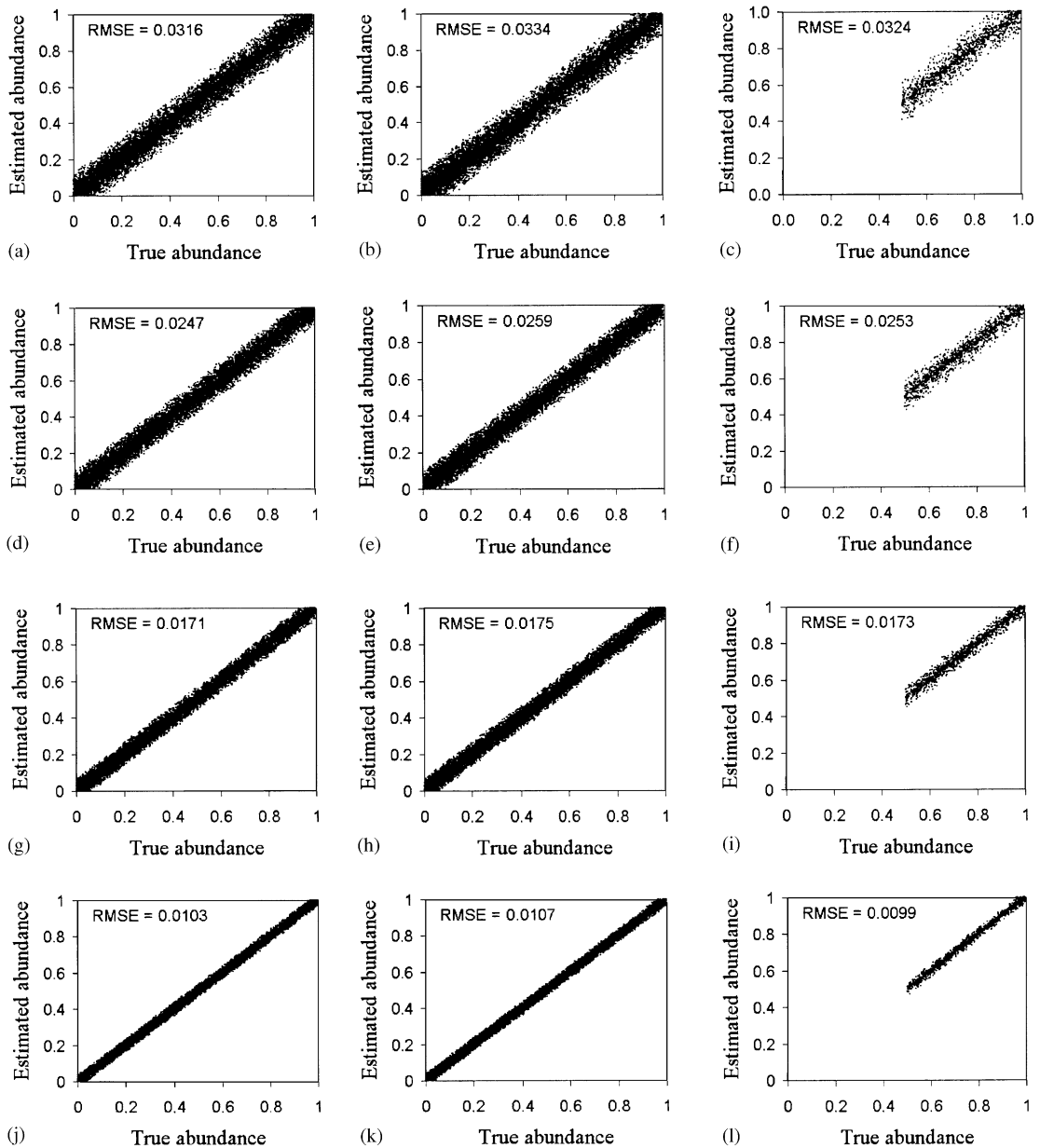


Fig. 9. Scatter-plots of the estimated versus true abundances for  $r_1$ ,  $r_2$  and  $r_3$ , respectively, obtained after applying PPI (a)–(c), N-FINDR (d)–(f), AMEE (g)–(i) and ADMP (j)–(l) methods to the simulated hyperspectral scene described in Fig. 8.

this experiment by AMEE and ADMP-based methods was provided by a range of 10 increasing square-shaped SEs with sizes ranging from  $3 \times 3$  pixels (51 m) up to  $21 \times 21$  pixels (357 m). This range was determined empirically after analyzing the width in pixels of ground-truth classes shown in Fig. 10. Before applying the above classifiers, a total of 20 channels from the water absorption and noisy bands (104–108, 150–163, 200) were removed from the original

220-channel image, leaving 200 spectral features for the experiments [56].

Figs. 11(a)–(d) show the results obtained after applying the WTA M/P converter to the mixed pixel classification output provided by PPI, N-FINDR, AMEE and ADMP-based methods, respectively. For quantitative purposes, Table 4 addresses the number of true and false positives, and the true and false positive rates resulting for each method and

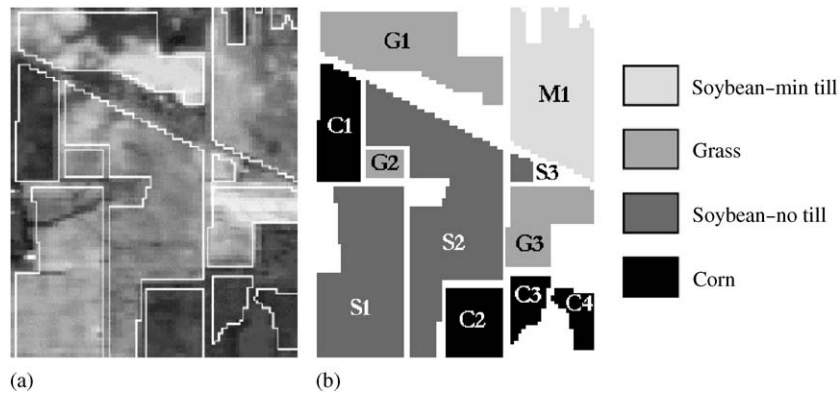


Fig. 10. (a) Portion of an AVIRIS hyperspectral dataset over NW Indiana's Indian Pines region; (b) Available ground-truth map with individual labeling of regions.

Table 3

Class description for AVIRIS hyperspectral data over Indiana's Indian Pines test site

Class name	Number of labeled pixels
Corn	702
Grass	955
Minimum-soybean	733
Soybean-no till	1885
Total	4275

class. True positives are pixels correctly assigned to a certain class, whereas false positives are pixels belonging to a certain class that are wrongly assigned to any of the other available classes. A simple visual comparison of the classification images shown in Figs. 11(a)–(d) with ground truth in Fig. 11(b) reveals that spectral-based methods (PPI and N-FINDR) are not able to provide a smooth mapping of regions spatially, and exhibit, instead, a significant amount of speckling. Although PPI provides a fairly good partitioning of the Corn class (regions labeled as C1–C4 in the ground-truth map), it has a problem when confusing the two soybean classes, especially in the region labeled as S2. This problem is quantitatively addressed in Table 4: Out of the 2065 pixels classified as minimum-soybean by PPI, 1486 were labeled as false positives and only 579 were labeled as true positives, resulting in a false positive rate of 0.42 for this class. As shown in Fig. 11(a), most of these false positive instances are produced at the S2 region (soybean-no till class). In addition, PPI presents problems in distinguishing grass from soybeans at the grass regions, denoted by G1–G3 in the ground-truth map. Most pixels in G2 and G3 are classified as soybean-no till, while grass tends to be confused with minimum-soybean in G1. As a result, the true positive rate for this class is only 0.34. For purposes of general performance, confusion between the two soybean classes is

not problematic; however, confusion between spectrally distinct materials such as grass and soybeans can be more troublesome. The confusion between grass and soybeans that plagues PPI is also a problem for the N-FINDR method, particularly at the G1, M1 and S3 regions. However, N-FINDR provides more accurate classification scores than PPI at the larger soybean-no till regions (S1 and S2), achieving a moderately high true positive rate of 0.71 and an acceptable false positive rate of 0.08 in this class, as reported in Table 4.

Compared to purely spectral methods (PPI and N-FINDR), spatial/spectral approaches (AMEE and ADMP-based) perform better in terms of true and false positive rates. As shown in Fig. 11(c), AMEE generates partitions that accurately represent structured regions in the image. However, some problems can be spotted at some of the larger regions, i.e. G1, G3, S1, S2 and M1. These problems are not unexpected because the AMEE algorithm, by construction, tends to emphasize local consistency spatially, by virtue of the consideration of SEs of progressively increased size at each pixel. A comparison of Fig. 11(c) with Fig. 11(d) provides justification that the ADMP-based method gives advantages in relation to the simple multi-scale spatial/spectral endmember extraction process performed by AMEE. Improvement in classification accuracy of the ADMP-based method with regards to AMEE, quantitatively reported in Table 4, can be attributed mainly to the adaptive selection of an optimum SE size for each pixel, which results in an optimization of the multi-scale morphological approach to endmember extraction. According to ground-truth, classification results produced by the proposed ADMP-based algorithm are characterized by an average true positive rate of 0.90 and an average false positive rate of 0.03. These average scores are considerably higher than those found by the remaining methods tested. Due to these results, we can deduce that the ADMP-based approach is able to provide a good characterization of general landscape conditions in a scene which reportedly represents a difficult classification problem due

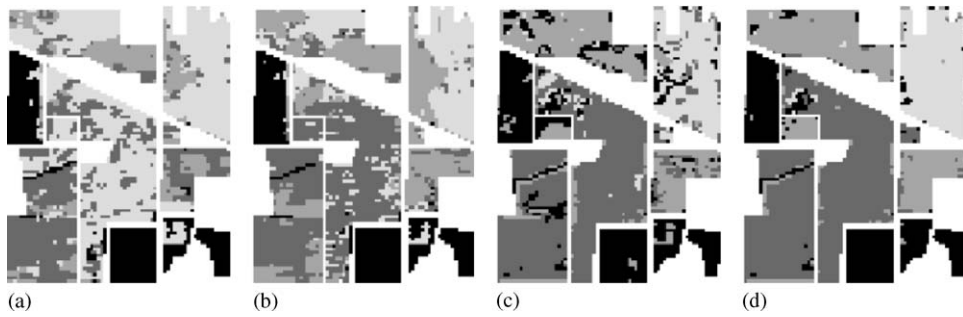


Fig. 11. Classification images for AVIRIS Indian Pines hyperspectral dataset, produced after applying the WTA M/P converter to the output provided by PPI (a), N-FINDR (b), AMEE (c), and ADMP-based (d) mixed pixel classifiers.

Table 4

Number of true positives (NTP), number of false positives (NFP), true positive rate (TPR), false positive rate (FPR) and total scores obtained after applying PPI, N-FINDR, AMEE and ADMP-based mixed pixel classifiers to AVIRIS Indian Pines hyperspectral dataset

Class name	PPI				N-FINDR				AMEE				ADMP-based			
	NTP	NFP	TPR	FPR	NTP	NFP	TPR	FPR	NTP	NFP	TPR	FPR	NTP	NFP	TPR	FPR
Corn	617	71	0.88	0.02	638	36	0.91	0.01	597	171	0.85	0.05	667	91	0.95	0.03
Grass	324	365	0.34	0.11	515	529	0.54	0.16	726	264	0.76	0.08	879	66	0.92	0.02
Min.-soybean	579	1486	0.79	0.42	462	453	0.63	0.13	601	212	0.82	0.06	682	124	0.93	0.04
Soybean-no till	829	237	0.44	0.10	1338	191	0.71	0.08	1621	119	0.86	0.05	1659	47	0.88	0.02
Total	2349	2159	0.54	0.14	2953	1209	0.69	0.09	3545	766	0.82	0.06	3887	328	0.90	0.03

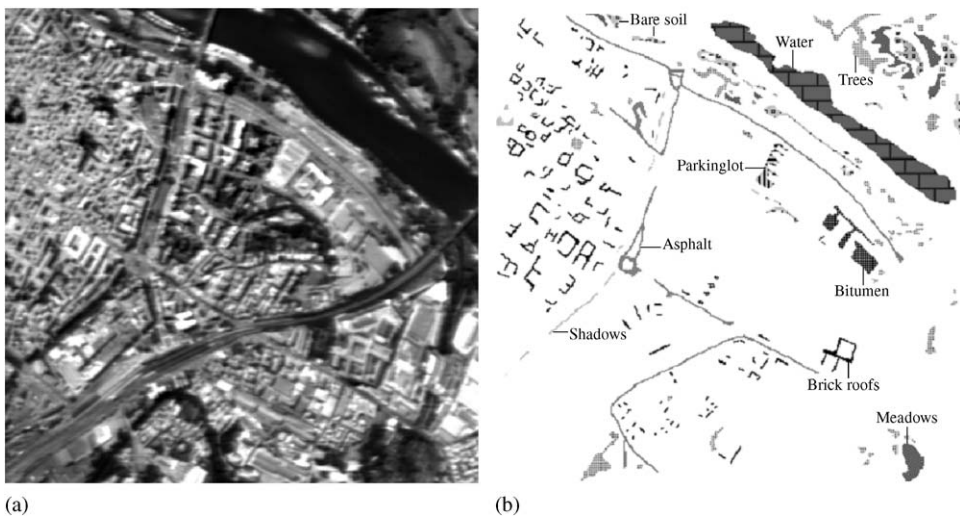


Fig. 12. (a) Band at 639 nm of a DAIS 7915 hyperspectral image comprising several urban features at the city of Pavia, Italy; (b) land-cover ground-truth classes.

to high spectral similarity between the different classes, low spatial resolution, and reduced SNR in comparison with current sensor standards. It is interesting to note that the proposed adaptative multi-scale approach seems to have a hierarchical effect. Large regions appear to have the same label, improving spatial localization for mapping purposes. It should be noted that the Indian Pines scene is dominated by large and spectrally homogeneous regions. As a result, a very simple behavior of morphological profiles was generally observed, where each feature had only one significant derivative maximum. Complex scenarios such as urban environments are characterized by features with several significant derivative maxima and nested regions. As a result, further experiments using real hyperspectral data collected over urban areas are required.

#### 4.2.2. Experiment with DAIS 7915 data comprising urban areas in Pavia, Italy

In this experiment, data from the DAIS 7915 airborne imaging spectrometer of DLR were used. The data were collected at 1500 m flight altitude over the city of Pavia, Italy, with ground resolution of 5 m and size of  $400 \times 400$  pixels ( $2000 \times 2000$  m). Fig. 12(a) shows the image collected at 639 nm by the DAIS 7915 imaging spectrometer, which reveals a dense residential area on one side of the river, as well as open areas and meadows on the other side. Ground-truth is available for several areas of the scene (see Fig. 12(b)), comprising the following land-cover classes (the number of labeled pixels in each class is addressed in Table 5): (1) water; (2) trees; (3) asphalt; (4) parking lot; (5) bitumen; (6) brick roofs; (7) meadows; (8) bare soil; (9) shadows.

A summary of the results obtained after applying the WTA M/P converter to different mixed-pixel classifiers is given in Table 6. As it can be seen in the table, the proposed ADMP-based method produces a moderate average true positive rate of 0.82 and an average false positive rate of 0.05. These results are better than those found after applying the PPI ( $L = 10^4$  iterations), N-FINDR and AMEE methods to this particular scene. It should be noted that the spatial domain explored in this experiment by both AMEE and ADMP-based methods was provided by a range of 8 increasing square-shaped SEs with sizes ranging from  $3 \times 3$  pixels (15 m) up to  $17 \times 17$  pixels (85 m), determined empirically after analyzing the width in pixels of ground-truth classes shown in Fig. 12. Although the application of the ADMP-based method leads to a more accurate characterization of urban features, the inherent complexity of the analyzed urban landscape prevents the proposed approach from obtaining optimal results.

In order to improve classification accuracy in this particular experiment, we have applied the proposed method with the modified ADSOMP algorithm (see Table 2), which is especially suited for analysis of directional features as reported in Section 3.3. As shown in Table 6, the incorporation of scale-orientation information by the proposed

Table 5  
Class description for DAIS 7915 hyperspectral data over Pavia city, Italy

Class name	Number of labeled pixels
Water	4290
Trees	2424
Asphalt	1699
Parking lot	288
Bitumen	685
Brick roofs	2238
Meadows	1245
Bare soil	1475
Shadows	241
Total	14585

ADSOMP-based method results in average true positive rate of 0.89 and average false positive rate of 0.02. Interestingly, the modified algorithm produces very accurate classification results for the classes dominated by small directional features: The asphalt, brick roofs, and shadows classes are characterized by true positive rates of 0.93 or higher, and false positive rates below 0.01, which represents a considerable improvement with respect to results found by the original ADMP-based algorithm and other methods. In addition, results for the water, trees and meadows classes are moderately better than those found by the original ADMP-guided implementation. It should be noted that these classes are dominated by wide objects of similar spectral properties. The incorporation of scale-orientation information also helps in characterizing large, oriented objects such as the river crossing the city centre. The remaining classes: bitumen, parking lot, and bare soil are given by a combination of homogeneous regions and directional features. When scale-orientation morphological profiles are applied to these image features, classification results are significantly better than those found by using scale-based morphological profiles with no orientation information. Overall, it has been shown in experiments that scale-based and scale-orientation morphological profiles are able to work efficiently at both local and global scales, providing a final classification output that is coherent in both spectral and spatial terms in complex, real-world scenarios.

## 5. Conclusions and future research

We have described a novel approach to perform unsupervised mixed pixel classification in hyperspectral images. The method uses an adaptative approach, based on extended morphological profiles and derivative analysis. This approach allows for the determination of an appropriate SE for each pixel of the scene by analyzing the spatial and spectral information in a combined manner. Once an

Table 6

True positive rate (TPR), false positive rate (FPR) and total scores obtained after applying PPI, N-FINDR, AMEE, ADMP-based and ADSOMP-based mixed pixel classifiers to a DAIS 7915 hyperspectral dataset over Pavia city, Italy

Class name	PPI		N-FINDR		AMEE		ADMP-based		ADSOMP-based	
	TPR	FPR	TPR	FPR	TPR	FPR	TPR	FPR	TPR	FPR
Water	0.68	0.06	0.81	0.10	0.85	0.04	0.86	0.01	0.92	0.01
Trees	0.69	0.09	0.75	0.15	0.74	0.11	0.84	0.05	0.88	0.03
Asphalt	0.73	0.12	0.71	0.14	0.69	0.09	0.77	0.04	0.95	0.01
Parking lot	0.61	0.08	0.67	0.09	0.82	0.08	0.87	0.02	0.90	0.00
Bitumen	0.64	0.11	0.71	0.13	0.80	0.09	0.85	0.02	0.89	0.01
Brick roofs	0.68	0.12	0.67	0.09	0.64	0.12	0.80	0.05	0.93	0.01
Meadows	0.72	0.08	0.71	0.12	0.79	0.07	0.79	0.04	0.86	0.03
Bare soil	0.63	0.09	0.61	0.11	0.73	0.10	0.81	0.04	0.88	0.01
Shadows	0.62	0.14	0.66	0.12	0.68	0.13	0.79	0.05	0.94	0.00
Total	0.68	0.10	0.73	0.11	0.76	0.09	0.82	0.04	0.89	0.02

optimum SE is selected, a morphological profile-based purity index function,  $\Pi(x, y)$ , is calculated at each image pixel position  $(x, y)$  by using residuals from extended opening- and closing-by-reconstruction operations. An evaluation of the proposed approach using simulated and real hyperspectral data has been presented and discussed. As demonstrated in the experiments, the method guarantees excellent performance when compared to other standard hyperspectral analysis methodologies. In particular, it gives a much better interpretation of mixed pixels than those methods that utilize the spectral information alone. The method has a hierarchical effect that improves spatial localization for general-purpose mapping applications. Also, it has been shown in experiments that the use of scale-orientation morphological profiles allows accurate modeling of complex analysis scenarios, such as urban environments. A drawback of the proposed approach concerns the necessity of looking at a range of increasing scale and orientation features, which may result in a heavy computational burden when processing high-dimensional data. This phenomenon is particularly important in the case of images with large and homogeneous regions. For this reason, the method presented is particularly suited for analysis of image scenes where small target objects or directional features must be retained. It is also well suited for images with spectrally similar materials and relatively low spatial resolution, which produces ambiguity in sub-pixel analysis.

Our current research focuses on the development of effective implementation strategies by the proposed approach with the use of hardware architectures. A systolic array design, susceptible of being implemented on field-programmable gate arrays, has already been developed and is currently under test in our laboratory. A detailed description of the above design, aimed at optimizing extended morphological operations, can be found in Ref. [57]. Massive parallel implementations using computer Beowulf-type

cluster architectures are also being explored in order to empower the methodology with real-time capabilities. A final topic of interest for future developments of the method consists in an evaluation of different distance measures (both linear and nonlinear) to be used in the extension of morphological operations.

### Acknowledgements

This research was supported by the European Commission through the project entitled “Generation of a test image to validate the performance of endmember extraction and hyperspectral un-mixing algorithms”, part of the DLR project “HySens-DAIS/ROSIS Imaging Spectrometers at DLR” (Contract Number HPRI-1999-00057). We would like to thank Paolo Gamba for providing the DAIS 7915 urban data set used in experiments. Contributions to this work by Andreas Müller, Rudolph Richter, Robert O. Green, Jose Moreno, Luis Alonso and John R. Miller are also gratefully acknowledged. In addition, the authors would like to express their gratitude to Michael Winter for providing an evaluation version of the N-FINDR algorithm, which was used to generate the results shown in this paper, and also for assistance in the use of his software and implementation of other methods.

### References

- [1] C.-I. Chang, *Hyperspectral Imaging: Spectral Detection and Classification*, Kluwer Academic/Plenum Publishers, New York, 2003.
- [2] R.O. Green, et al., *Imaging spectroscopy and the airborne visible/infrared imaging spectrometer (AVIRIS)*, *Remote Sens. Environ.* 65 (1998) 227–248.
- [3] D. Landgrebe, *Hyperspectral image data analysis*, *IEEE Signal Process. Mag.* 19 (2002) 17–28.

- [4] X. Jia, J.A. Richards, D.E. Ricken, *Remote Sensing Digital Image Analysis: An Introduction*, Springer, Berlin, 1999.
- [5] F. Kruse, A. Lefkoff, J.W. Boardman, K. Heidebrecht, A. Shapiro, P. Barloon, A. Goetz, The spectral image processing system (SIPS)—interactive visualization and analysis of imaging spectrometer data, *Remote Sens. Environ.* 44 (1993) 145–163.
- [6] Q. Du, C.-I. Chang, Linear constrained distance-based discriminant analysis for hyperspectral image classification, *Pattern Recognition* 34 (2001) 361–373.
- [7] C.-H. Chen, T.-M. Tu, Computation reduction of the maximum likelihood classifier using the Winograd identity, *Pattern Recognition* 29 (1996) 1213–1220.
- [8] P. Martínez, R.M. Pérez, P.L. Aguilar, A. Plaza, Systolic SOM neural network for hyperspectral image classification, in: D. Zhang, S.K. Pal (Eds.), *Neural Networks and Systolic Array Design*, World Scientific, Singapore, 2002, pp. 193–204.
- [9] W.H. Bakker, K.S. Schmidt, Hyperspectral edge filtering for measuring homogeneity of surface cover types, *ISPRS J. Photogramm. Remote Sens.* 56 (2002) 246–256.
- [10] N. Keshava, J.F. Mustard, Spectral unmixing, *IEEE Signal Process. Mag.* 19 (2002) 44–57.
- [11] R.S. Rand, D.M. Keenan, A spectral mixture process conditioned by Gibbs-based partitioning, *IEEE Trans. Geosci. Remote Sens.* 39 (2001) 1421–1434.
- [12] T.-M. Tu, H.-C. Shyu, C.-H. Lee, C.-I. Chang, An oblique subspace projection approach for mixed pixel classification in hyperspectral images, *Pattern Recognition* 32 (1999) 1399–1408.
- [13] C.C. Borel, S.A.W. Gerstl, Nonlinear spectral mixing models for vegetative and soil surfaces, *Remote Sens. Environ.* 47 (1994) 403–416.
- [14] P.M. Mather, Land cover classification revisited, in: P.M. Atkinson, N.J. Tate (Eds.), *Advances in Remote Sensing and GIS Analysis*, Wiley, Chichester, West Sussex, 1999.
- [15] D. Heinz, C.-I. Chang, Fully constrained least squares linear mixture analysis for material quantification in hyperspectral Imagery, *IEEE Trans. Geosci. Remote Sens.* 39 (2000) 529–545.
- [16] J.W. Boardman, F.A. Kruse, R.O. Green, Mapping target signatures via partial unmixing of AVIRIS data, *Summaries of the Sixth JPL Airborne Earth Science Workshop*, Pasadena, CA, 1995.
- [17] A. Green, M. Berman, P. Switzer, M. Craig, A transformation for ordering multi-spectral data in terms of image quality with implications for noise removal, *IEEE Trans. Geosci. Remote Sens.* 26 (1988) 65–74.
- [18] M.E. Winter, N-FINDR: An algorithm for fast autonomous spectral end-member determination in hyperspectral data, *Proceedings of the SPIE Imaging Spectrometry V*, San Diego, CA, 1999.
- [19] V. Madhok, D. Landgrebe, Spectral-spatial analysis of remote sensing data: an image model and a procedural design, Ph.D. Dissertation, School of Electrical Engineering and Computer Science, Purdue University, Lafayette, IN, 1998.
- [20] Q. Jackson, D. Landgrebe, Adaptive Bayesian contextual classification based on Markov random fields, *IEEE Trans. Geosci. Remote Sens.* 40 (2002) 2454–2463.
- [21] A. Plaza, P. Martínez, R. Pérez, J. Plaza, Spatial/spectral endmember extraction by multidimensional morphological operations, *IEEE Trans. Geosci. Remote Sens.* 40 (2002) 2025–2041.
- [22] A. Plaza, P. Martínez, J.A. Gualtieri, R.M. Pérez, Automated identification of endmembers from hyperspectral images using mathematical morphology, *Proceedings of the Eighth SPIE International Symposium on Remote Sensing*, Toulouse, France, 2001.
- [23] A. Plaza, P. Martínez, J.A. Gualtieri, R.M. Pérez, Spatial/spectral identification of endmembers from AVIRIS data using mathematical morphology, *Proceedings of the X NASA/Jet Propulsion Laboratory Airborne Earth Science Workshop*, Pasadena, CA, 2001.
- [24] A. Plaza, P. Martínez, R. Pérez, J. Plaza, Hyperspectral image analysis by scale-orientation morphological profiles, *Proceedings of the X SPIE International Symposium on Remote Sensing*, Barcelona, Spain, 2003.
- [25] P. Soille, M. Pesaresi, Advances in mathematical morphology applied to geoscience and remote sensing, *IEEE Trans. Geosci. Remote Sens.* 40 (2002) 2042–2055.
- [26] G. Flouzat, O. Amram, F. Laporterie, S. Cherchali, Multi-resolution analysis and reconstruction by a morphological pyramid in the remote sensing of terrestrial surfaces, *Signal Process.* 81 (2001) 2171–2185.
- [27] J. Serra, *Image Analysis and Mathematical Morphology*, Academic, New York, 1982.
- [28] S.R. Sternberg, Grayscale morphology, *Comput. Vision Graphics Image Process.* 35 (1986) 333–355.
- [29] R.M. Haralick, S.R. Sternberg, X. Zhuang, Image analysis using mathematical morphology, *IEEE Trans. Pattern Anal. Mach. Intell.* 9 (1987) 532–550.
- [30] P. Soille, *Morphological Image Analysis—Principles and Applications*, Springer, Berlin, 1999.
- [31] G. Louverdis, M.I. Vardavoulia, I. Andreadis, Ph. Tsalides, A new approach to morphological color processing, *Pattern Recognition* 35 (2002) 1733–1741.
- [32] V. Barnett, The ordering of multivariate data, *J.R. Statist. Soc. A* 139 (1976) 318–355.
- [33] J. Goutsias, H.J.A.M. Heijmans, K. Sivakumar, Morphological operators for image sequences, *Comput. Vision Image Understanding* 62 (1995) 326–346.
- [34] M. Comer, E. Delp, Morphological operations for color image processing, *J. Electron. Imag.* 8 (1999) 279–289.
- [35] M. Pesaresi, J.A. Benediktsson, A new approach for the morphological segmentation of high resolution satellite imagery, *IEEE Trans. Geosci. Remote Sens.* 39 (2001) 309–320.
- [36] J. Goutsias, H.J.A.M. Heijmans, *Fundamenta morphologicae mathematicae*, *Fund. Inf.* 41 (1999) 1–30.
- [37] A. Müller, A. Hausold, P. Strobl, HySens—DAIS/ROSIIS imaging spectrometers at DLR, *Proceedings of the Eighth SPIE International Symposium on Remote Sensing*, Toulouse, France, 2001.
- [38] T. Chen, Q.H. Wu, R. Rahmani-Torkaman, J. Hughes, A pseudo top-hat mathematical morphological approach to edge detection in dark regions, *Pattern Recognition* 35 (2002) 199–210.
- [39] F. Cheng, A.N. Venetsanopoulos, Adaptive morphological operators, fast algorithms and their applications, *Pattern Recognition* 33 (2000) 917–933.
- [40] L. Vincent, Morphological grayscale reconstruction in image analysis: applications and efficient algorithms, *IEEE Trans. Image Process.* 2 (1993) 176–201.

- [41] I. Bloch, Geodesic balls in a fuzzy set and fuzzy geodesic mathematical morphology, *Pattern Recognition* 33 (2000) 897–905.
- [42] P. Soille, H. Talbot, Directional morphological filtering, *IEEE Trans. Pattern Anal. Mach. Intell.* 23 (2001) 1313–1329.
- [43] P.K. Sahoo, S. Soltani, A.K.C. Wong, A survey of thresholding techniques, *Comput. Vision, Graphics Image Process.* 41 (1988) 233–260.
- [44] N. Otsu, A threshold selection method from gray-level histograms, *IEEE Trans. Syst. Man Cybernet.* 9 (1979) 62–66.
- [45] M. Faraklioti, M. Petrou, Illumination invariant unmixing of sets of mixed pixels, *IEEE Trans. Geosci. Remote Sens.* 39 (2001) 2227–2234.
- [46] A. Ifarraguerri, C.-I. Chang, Multi-spectral and hyperspectral image analysis with projection pursuit, *IEEE Trans. Geosci. Remote Sens.* 37 (1999) 756–770.
- [47] G.D. Robinson, H.H. Gross, J.R. Schott, Evaluation of two applications of spectral mixing models to image fusion, *Remote Sens. Environ.* 71 (2000) 272–281.
- [48] J.C. Harsanyi, C.-I. Chang, Hyperspectral image classification and dimensionality reduction: an orthogonal subspace projection approach, *IEEE Trans. Geosci. Remote Sens.* 32 (1994) 779–785.
- [49] T. Rashed, J. Weeks, M. Gadalla, A. Hill, Revealing the anatomy of cities through spectral mixture analysis of multi-spectral satellite imagery: a case study of the Greater Cairo region, Egypt, *Geocarto Int.* 16 (2001) 5–16.
- [50] Purdue Univ. Multispec homepage. Available: <ftp://ftp.ecn.purdue.edu/biehl/MultiSpec/92AV3C>.
- [51] J.A. Palmason, J.A. Benediktsson, K. Arnason, Morphological transformations and feature extraction for urban data with high spectral and spatial resolution, Proceedings of the IEEE International Geoscience Remote Sensing Symposium, Toulouse, France, 2003.
- [52] C.-I. Chang, H. Ren, An experiment-based quantitative and comparative analysis of target detection and image classification algorithms for hyperspectral imagery, *IEEE Trans. Geosci. Remote Sens.* 38 (2000) 1044–1063.
- [53] A.J. Simon, A model for biological winner-take-all neural competition employing inhibitory modulation of NMDA-mediated excitatory gain, *Neurocomputing* 26 (1999) 587–592.
- [54] R.O. Green, B. Pavri, J. Faust, O. Williams, AVIRIS radiometric laboratory calibration, inflight validation and a focused sensitivity analysis in 1998, Proceedings of the Eighth NASA/Jet Propulsion Laboratory Airborne Earth Science Workshop, Pasadena, CA, 1999.
- [55] S. Tadjudin, D. Landgrebe, Covariance estimation with limited training samples, *IEEE Trans. Geosci. Remote Sens.* 37 (1999) 2113–2118.
- [56] V. Haertel, D. Landgrebe, On the classification of classes with nearly equal spectral responses in remote sensing hyperspectral data, *IEEE Trans. Geosci. Remote Sens.* 37 (1999) 2374–2386.
- [57] P.L. Aguilar, A. Plaza, R. Perez, P. Martinez, Morphological endmember identification and its systolic array design, in: D. Zhang, S.K. Pal (Eds.), *Neural Networks and Systolic Array Design*, World Scientific, Singapore, 2002, pp. 47–69.

**About the Author**—ANTONIO PLAZA received the Ph.D. degree in Computer Science from the University of Extremadura, Caceres, Spain, in 2002. Dr. Plaza has been Associate Professor with the Computer Science Department, University of Extremadura, Spain, since 2000. He has held Visiting Researcher positions at the Applied Information Sciences Branch, NASA/Goddard Space Flight Center, Greenbelt, MD, the Department of Electrical Engineering, University of Maryland, College Park, MD, and the AVIRIS Data Facility, NASA/Jet Propulsion Laboratory, Pasadena, CA. His main research interests span computer vision, image processing, pattern recognition, and development and efficient implementation of hyperspectral image analysis algorithms on massively parallel computing facilities and VLSI hardware-based computer architectures. He is currently serving as a reviewer for the IEEE Transactions on Geoscience and Remote Sensing and IEEE Transactions on Image Processing journals.

**About the Author**—PABLO MARTINEZ received the Ph.D. degree in Physics from the University of Granada, Spain, in 1992. Dr. Martínez has been a Professor of Computer Science at University of Extremadura, Spain, since 1985. He is the Head Scientist of the Neural Networks and Signal Processing Group (GRNPS). He has held Visiting Researcher positions at the Applied Information Sciences Branch, NASA/Goddard Space Flight Center, Greenbelt, MD, and the Department of Electrical Engineering, University of Maryland, College Park, MD. His main research interests include remote sensing, digital image analysis, hardware-based architectures, operating systems management and configuration, and neural network-based pattern recognition.

**About the Author**—ROSA PEREZ received the Ph.D. degree in Computer Science from the Polytechnic University of Madrid, Spain, in 1995. Dr. Pérez has been a Professor of Computer Science at the Computer Science Department, University of Extremadura, Spain, since 1985. Her main research interests include neural networks, systolic array- and FPGA-based design, pattern recognition, and signal processing.

**About the Author**—JAVIER PLAZA received the M.Sc. degree in Computer Science from the University of Extremadura, Spain, in 2002, where he is currently pursuing the Ph.D. degree. Mr. Plaza is an Assistant Professor at the Computer Science Department, University of Extremadura, Spain. His current research work is focused on the development of efficient implementations of nonlinear mixture model-based algorithms for abundance estimation of materials in hyperspectral scenes. He is also involved in the design and configuration of commodity cluster computing architectures for high-performance hyperspectral analysis. Other major research interests include development of quantitative and comparative applications for remote sensing, and design of web-based applications for hyperspectral image processing.